Solid State Ionics 255 (2014) 60–64

Contents lists available at ScienceDirect

Solid State Ionics

journal homepage: www.elsevier.com/locate/ssi

Lithium ion insertion properties of nanocrystalline anatase titanium oxides prepared from peroxo-polytitanic acid

Isao Tsuyumoto *, Kazuki Kobayashi

Department of Applied Chemistry, College of Bioscience and Chemistry, Kanazawa Institute of Technology, 7-1 Ohgigaoka, Nonoichi, Ishikawa 921-8501, Japan

ARTICLE INFO

Article history:
Received 17 June 2013
Received in revised form 31 October 2013
Accepted 27 November 2013
Available online xxxx

Keywords:
Lithium
Titanium oxide
Battery
Anatase
Peroxide

ABSTRACT

Peroxo-polytitanic acid (Ti-iPA) solution was obtained by using a reaction between metallic Ti powder and 30 wt.% aq. H_2O_2. Amorphous titanium oxide was prepared by drying Ti-iPA solution at 115 °C, and nanocrystalline anatase titanium oxide was prepared by heating the amorphous phase at 300–500 °C. The crystal structure was the same as that of the conventional anatase form. The anatase titanium oxide obtained by heating at 300 °C for 5 h with an average particle size of 25 nm showed the capacity of 158 mA h/g as negative electrode for lithium ion batteries. The capacity was increased with increasing the heating time at 300 °C and reduced with increasing the heating temperature to 400–500 °C. The lithium insertion/deinsertion performance was enhanced by heating at 300 °C because lattice defects were reduced without crystal growth and aggregation. We also calculated site energy distribution from the deconvolution of experimental discharge curves, and discussed the relationship between the structure and the insertion site.

1. Introduction

Titanium oxides have attracted much attention as negative electrode materials of lithium ion batteries because they accommodate lithium ion and show lithium diffusivity in the host lattices [1–4]. Many researchers have reported new preparation methods of titanium oxides such as anatase [5–10], rutile [11,12], hollandite [13], ramsdellite [14], TiO_2 (B) [15,16], amorphous [17], and have discussed their electrochemical lithium insertion/deinsertion properties in relation to the crystal structure, crystallinity, particle size and surface morphology [18]. The earlier reports mostly indicated that large surface area compatible with few lattice defects is essential to the good lithium insertion/deinsertion performance. Nanocrystalline titanium oxides have been reported to be appropriate for the lithium insertion materials, because the large surface area and small particle diameter favor the lithium diffusion across the electrolyte/electrode interface and inside the particles. Soft-chemical processes such as the hydrothermal method [19–22], the sol–gel method [23,24], and the precursor pyrolysis method [25,26] have advantages over the conventional solid state reactions to prepare such homogeneous nanocrystalline titanium oxides.

In our previous study, we have developed new synthetic routes of metal oxides from peroxo-metallic acid obtained by reaction between metallic powder and concentrated hydrogen peroxide solution [27–36]. For example, peroxo-polytungstic acid is obtained by vigorous reaction between metallic tungsten powder and hydrogen peroxide solution [36], and its salts with alkalis yields novel tungsten bronzes at 500–700 °C [33]. Similarly molybdenum, niobium, vanadium and titanium powders react with hydrogen peroxide and yield the correspondent peroxo-metallic acids. Since the reaction of the titanium powder with hydrogen peroxide was markedly slow compared with the other metals, we have accelerated the reaction by concentrating the hydrogen peroxide up to 70 wt.% and have obtained the peroxo-polytitaninic solution (titanium isopolyacid, Ti-iPA) in 6 h. Furthermore, we have successfully prepared nanosized tetragonal $BaTiO_3$ from the salt of peroxo-polytitanic acid and $Ba(OH)_2$ [29]. To prepare Ti-iPA solution is a very useful method to solubilize titanium into aqueous solution, and we found that its dry residue yields amorphous and nanocrystalline anatase titanium oxides by heating at relatively low temperatures. In the present study, we investigated lithium insertion/deinsertion properties of amorphous and nanocrystalline anatase titanium oxides prepared from Ti-iPA solutions under various conditions. Furthermore, we also present the energy distribution of lithium insertion site calculated from the experimental charge/discharge curves using a numerical deconvolution technique based on the theoretical relationship between the charge/discharge curves and the energy distribution of lithium insertion site in host materials.

2. Experimental

2.1. Sample preparation

Metallic Ti powder (0.36 g, 45 μm particle size, as received from Wako Pure Chemical Industries Ltd., Osaka, Japan) was dissolved in 150 mL of 30 wt.% aq. H_2O_2 solution (Wako Pure Chemical Industries Ltd., Osaka, Japan) at 20 °C with stirring. The dissolving reaction proceeded mildly with the emission of oxygen gas, and a yellow transparent solution of peroxo-polytitanic acid (denoted as Ti-iPA where

* Corresponding author.
E-mail address: tsuyu@neptune.kanazawa-it.ac.jp (I. Tsuyumoto).

0167-2738/$ – see front matter © 2013 Elsevier B.V. All rights reserved.
http://dx.doi.org/10.1016/j.ssi.2013.11.048

iPA stands for isopolyacid) was obtained in 24 h. After removing insolubles by filtration, Ti-iPA solution was dried at 115 °C for 24 h to yield yellow amorphous powder. Amorphous and nanocrystalline TiO_2 were prepared by heating the yellow powder as a precursor in air at the desired temperatures specified by thermal and structural analyses.

2.2. Characterization

The thermal behavior of the amorphous precursor was investigated by thermogravimetry (TG) and differential thermal analysis (DTA; DTG-50 Shimadzu, Kyoto, Japan) in air at a heating rate of 20 °C/min. The XRD patterns of the products were measured with a diffractometer (XD-D1, Shimadzu, Kyoto, Japan) using graphite-monochromatized Cu $K\alpha$ radiation ($\lambda = 0.15406$ nm) at 30 kV and 30 mA. The X-ray profiles were collected between 2° and 120° of 2θ angles with a step interval of 0.02° and a count time of 1 s/step. The crystalline parameters were refined by the Rietveld method using the RIETAN-FP program [37], and the crystallite sizes were determined by the Scherrer equation. For lithium deinsertion/insertion measurements, each sample of 16.6–16.7 mg was intimately ground with acetylene black (AB) at a weight ratio of 1:1, and the composite, after mixing with 15.0 mg of polytertrafluoroethylene (PTFE) as a binder, was pressed onto a copper mesh. The Ag/Ag^+ electrode for non-aqueous solvent (RE-7, ALS Corporation Ltd., Tokyo, Japan) was used as a reference electrode, and its potential was determined at 3.84 V vs Li. The counter electrode was a mixture of 61 mg $LiCoO_2$, 12 mg AB, and 5 mg poly(vinylidene difluoride) (PVDF) as a binder. The active material in the counter electrode was three times in excess compared to that in the working electrode. The lithium deinsertion/insertion measurements were carried out in the galvanostatic mode at 3.0 mA (1.08 C rate) in the range 1.0–3.5 V (vs Li). Discharge curves were also measured at 0.06 mA (0.022 C rate) in order to use as OCV (open circuit voltage) curves in theoretical calculations.

3. Results and discussion

3.1. Formation of amorphous and nanocrystalline TiO_2 from Ti-iPA solution

Fig. 1 shows the TG and DTA curves for the residue obtained by drying Ti-iPA solution at room temperature. The weight decreased monotonously by 25% up to around 400 °C and remained almost constant over around 400 °C. An exothermic peak appeared at 396 °C, around which the weight ceased to decrease. These indicate that the condensation of hydroxyl group, the decomposition of peroxo group, and the volatilization of H_2O and H_2O_2 proceed continuously up to around 400 °C, and that crystallization occurs at around 396 °C after the completion of the release of H_2O, H_2O_2 and O_2. Fig. 2 shows the XRD patterns of amorphous titanium oxide obtained at the residue of Ti-iPA solution dried at 115 °C for 24 h and of nanocrystalline anatase TiO_2 obtained by

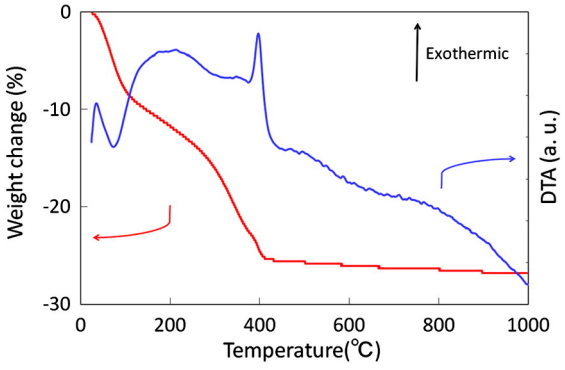

Fig. 1. DTA and TG curves for the residue obtained by drying Ti-iPA solution at room temperature.

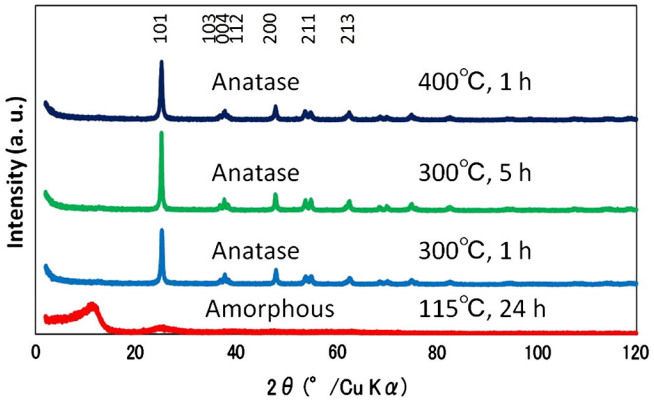

Fig. 2. Powder XRD patterns of titanium oxides prepared from Ti-iPA. Amorphous phase is the residue of Ti-iPA aq. dried at 115 °C for 24 h, and nanocrystalline anatase forms are obtained by heating the amorphous phase.

heating the amorphous titanium oxide at 300 or 400 °C. The nanocrystalline anatase TiO_2 was formed by heating the amorphous titanium oxide under such conditions as at 290 °C for 10 h or at 300–500 °C for 1 h or more, while the products remained amorphous after heating at 280 °C for 1–10 h or at 290 °C for 1–5 h. In the XRD patterns, the crystallization into anatase form occurred in the temperature range of 290–300 °C, whereas the exothermic crystallization peak was observed around 396 °C in the DTA curve at the heating rate of 20 °C/min. This discrepancy is due to the difference of the heating time. The crystallization was triggered below 396 °C, because the condensation of hydroxyl group, the decomposition of peroxo group, and the volatilization of H_2O and H_2O_2 in the amorphous phase were completed by prolonging the heating time to 10 h at 290 °C or 1 h at 300 °C. Table 1 shows structural parameters and crystallite sizes refined by the Rietveld method. The space group, $I4_1/amd$, and the site coordinates were the same as that of the conventional anatase TiO_2 [19,38]. As mentioned above, the amorphous phase crystallized into the anatase form over around 300 °C. The crystallite sizes of heating time 1 h and 5 h at 300 °C were 22 nm and 25 nm, respectively, indicating that crystal growth hardly proceeds around 300 °C. Elevating the heating temperature to 400 °C and 500 °C also resulted in a little increase in crystallite size.

3.2. Lithium insertion and deinsertion properties

Fig. 3 shows charge/discharge curves of the titanium oxides prepared from Ti-iPA. The amorphous titanium oxide prepared by heating at 115 °C for 24 h showed a steep potential change without a plateau region by lithium insertion and deinsertion, as shown in Fig. 3(a). The amorphous titanium oxides prepared by heating at 280 °C for 1 h, 5 h, and 10 h also showed the same charge/discharge curves as the one

Table 1
Structural parameters refined by the Rietveld method and crystallite sizes. Tetragonal, space group; $I4_1/amd$ (144). All occupancies are fixed at unity.

Heating condition	Lattice parameter	Site coordinate and atomic position	Crystallite size
300 °C, 1 h	$a = 3.789$, $c = 9.512$	Ti 4*a* (0, 3/4, 1/8) O 8*e* (0, 1/4, *u*), $u = 0.208$	22 nm
300 °C, 5 h	$a = 3.796$, $c = 9.527$	Ti 4*a* (0, 3/4, 1/8) O 8*e* (0, 1/4, *u*), $u = 0.206$	25 nm
400 °C, 1 h	$a = 3.793$, $c = 9.521$	Ti 4*a* (0, 3/4, 1/8) O 8*e* (0, 1/4, *u*), $u = 0.207$	22 nm
400 °C, 5 h	$a = 3.787$, $c = 9.512$	Ti 4*a* (0, 3/4, 1/8) O 8*e* (0, 1/4, *u*), $u = 0.205$	26 nm
500 °C, 1 h	$a = 3.786$, $c = 9.515$	Ti 4*a* (0, 3/4, 1/8) O 8*e* (0, 1/4, *u*), $u = 0.208$	25 nm
500 °C, 5 h	$a = 3.790$, $c = 9.524$	Ti 4*a* (0, 3/4, 1/8) O 8*e* (0, 1/4, *u*), $u = 0.207$	27 nm

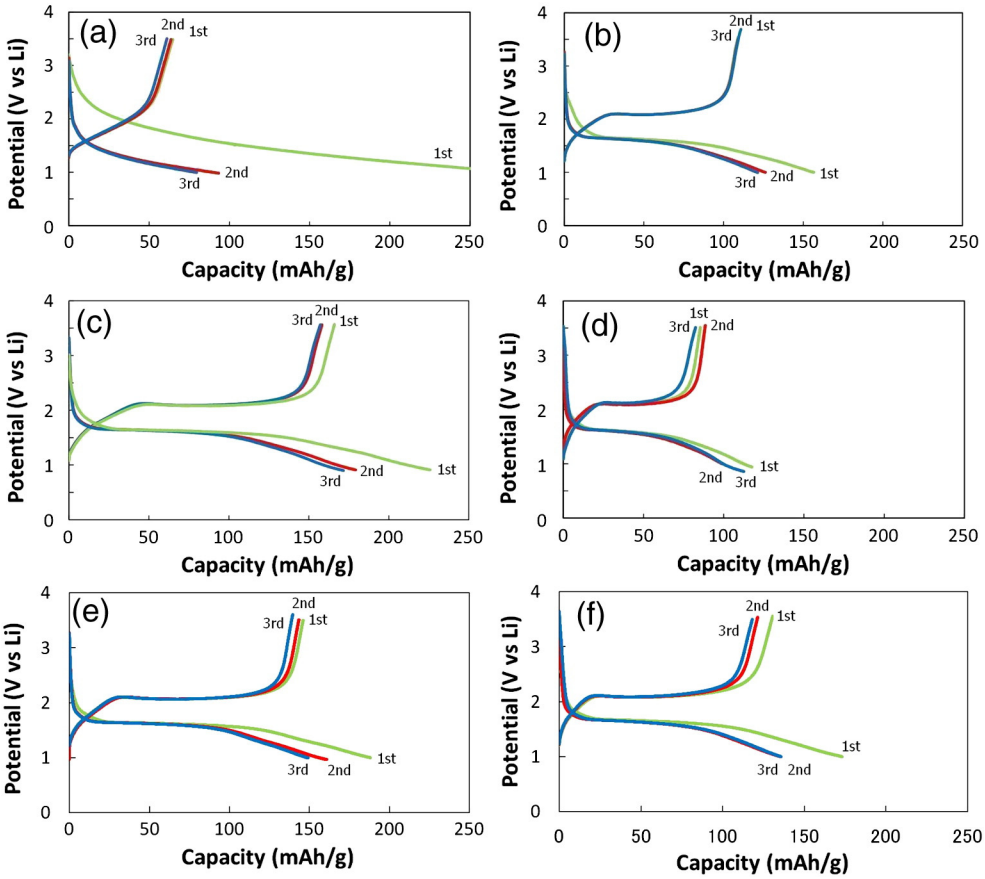

Fig. 3. Charge/discharge curves of the titanium oxides prepared from Ti-iPA by heat treatment of (a) 115 °C, 24 h; (b) 300 °C, 1 h; (c) 300 °C, 5 h; (d) 400 °C, 1 h; (e) 400 °C, 5 h; and (f) 500 °C, 5 h.

prepared at 115 °C. The capacities were about 60 mA h/g much lower than the theoretical value 168 mA h/g, suggesting that the lithium insertion sites are heterogeneous and more than half of them are unsuitable for lithium insertion due to spatial or energetic reason. The steep change of the potential also suggests the heterogeneous lithium insertion sites in the amorphous phase. These are consistent with the experimental fact that the crystallization occurs after the completion of the release of H_2O, H_2O_2 and O_2. The remaining hydroxyl and peroxo groups and the caged molecules such as H_2O, H_2O_2 and O_2 in the amorphous matrix probably make the insertion sites spatially or energetically inaccessible to the lithium. Fig. 3(b)–(f) shows charge/discharge curves of nanocrystalline anatase TiO_2 obtained by heating at 300–500 °C. A plateau region was observed for all the nanocrystalline TiO_2, indicating that the insertion sites are homogeneously formed in the nanocrystals. The capacity varied depending on the preparative conditions. The capacity was increased from 109 mA h/g to 158 mA h/g with increasing the heating time from 1 h to 5 h at 300 °C. On the contrary, the capacity was decreased to 143 mA h/g and 121 mA h/g with elevating the heating temperature to 400 °C and 500 °C, respectively. Interestingly, the anatase TiO_2 obtained at 300 °C for 5 h showed the largest capacity 158 mA h/g at rather high rate 1.08 C, and this is close to the theoretical value 168 mA/g. Similar performance has been reported for anatase TiO_2 with crystallite size 30–40 nm prepared at 400 °C from oxalatopolytitanate by Yagi et al. [7], but the current density, 25 mA/g, for their case was much smaller than that for our case, 181 mA/g. We can say that we first achieved the capacity 158 mA h/g at rate 1.08 C using the anatase TiO_2 obtained at 300 °C. Elevating the heating temperature to 400–500 °C brought about the reduction of the capacity, because crystal growth and aggregation to form secondary particles are not favorable for the diffusion of lithium ion into and out of the particles. Prolonging the heating time from 1 h to 5 h at 300 °C contributed to the reduction of lattice defects without crystal growth and secondary particle formation. Heating the amorphous precursor at 300 °C is the most appropriate route to prepare nanocrystalline TiO_2 for lithium insertion and deinsertion, because crystal growth and aggregation are suppressed and lattice defects are reduced at 300 °C. Low temperature process around 300 °C is appropriate for preparation of lithium insertion materials because it can provide nanocrystals with fewer lattice defects.

3.3. Theoretical relationship between site energy distribution and OCV curve

The electrode potential E (vs. Li) of lithium insertion materials is determined by the chemical potential difference between the inserted Li in host electrode $\mu_{Li,\ host}$ and the Li metal electrode $\mu_{Li,\ metal}$. When we set the chemical potential of the Li metal electrode $\mu_{Li,\ metal}$ at zero and consider the electrode potential E and the chemical potential of the inserted Li $\mu_{Li,\ host}$ as a function of Li content x in host electrode, the electrode potential is

$$E(x) = -\frac{\mu_{Li,host}(x)}{F}, \tag{1}$$

where F is the Faraday constant. Thus, the theoretical OCV curves are derived by the calculation of the chemical potential of Li in host electrode as a function of Li content x.

If the host material has insertion sites with homogeneous site energy $\varepsilon(<0)$ and total number N, and n sites among N are occupied by inserted Li, the internal energy change by the insertion is

$$\Delta U = n\varepsilon, \tag{2}$$

and the entropy change by the insertion is

$$\Delta S = k \ln \frac{N!}{n!(N-n)!}, \tag{3}$$

where k is the Boltzmann constant. Here we neglected repulsive forces among the inserted Li ions. In the present case, ΔH is considered to be equal to ΔU, because the volume change is negligibly small. The Gibbs energy change is

$$\Delta G = n\varepsilon - kT \ln \frac{N!}{n!(N-n)!}. \tag{4}$$

The chemical potential $\mu_{\mathrm{Li,\ host}}$ is obtained by differentiating Eq. (4) with respect to n as

$$\mu_{\mathrm{Li,host}}(x) = \varepsilon + kT \ln \frac{x}{1-x}, \tag{5}$$

where $x = n/N$ [39]. This equation bears close analogy to the Langmuir adsorption isotherm.

Let us consider a host material whose site energy has a wide distribution. In the case of amorphous host materials, innumerable kinds of insertion sites exist and each site energy is different from the other kinds of sites in varying degrees. The inserted Li is distributed among the sites so that the chemical potential of Li in each site becomes equal to each other.

If we denote each site energy by $\varepsilon_1, \varepsilon_2, \varepsilon_3, \cdots$ and the occupancy of each site by $f_1, f_2, f_3, \cdots$, the chemical potential of Li in each site is equally given by

$$\begin{aligned} \mu &= \varepsilon_1 + kT \ln \frac{f_1}{1-f_1} \\ &= \varepsilon_2 + kT \ln \frac{f_2}{1-f_2} \\ &= \varepsilon_3 + kT \ln \frac{f_3}{1-f_3} \\ &\quad \cdots. \end{aligned} \tag{6}$$

By transforming Eq. (6), we obtain

$$f_{\mathrm{i}} = \frac{1}{1 + \exp\left(-\frac{\mu-\varepsilon_{\mathrm{i}}}{kT}\right)} \quad (\mathrm{i} = 1, 2, 3, \cdots). \tag{7}$$

This equation indicates that the inserted Li obeys the Fermi distribution function in each site. If we denote the number of each site by $N_1, N_2, N_3, \cdots$, the number of each occupied site by $n_1, n_2, n_3, \cdots$, and the total number of the occupied sites by n, we obtain

$$n = \sum \frac{N_{\mathrm{i}}}{1 + \exp\left(-\frac{\mu-\varepsilon_{\mathrm{i}}}{kT}\right)} \quad (\mathrm{i} = 1, 2, 3, \cdots). \tag{8}$$

If we define a density function $g(\varepsilon) = dN(\varepsilon) / d\varepsilon$ by assuming that N_{i} shows a continuous distribution as a function of ε_{i}, Eq. (8) gives

$$n = \int_{-\infty}^{\infty} \frac{g(\varepsilon)}{1 + \exp\left(-\frac{\mu-\varepsilon}{kT}\right)} d\varepsilon. \tag{9}$$

Eq. (9) is a theoretical derivation of OCV curves, because the capacity corresponds to n and the potential to $-\mu/e$. It is interesting to note that the capacity is a convolution of the density function $g(\varepsilon)$ and the Fermi function

$$f(x) = \frac{1}{1 + \exp\left(-\frac{x}{kT}\right)}, \tag{10}$$

as

$$n(\mu) = \int_{-\infty}^{\infty} f(\mu-\varepsilon) g(\varepsilon) d\varepsilon. \tag{11}$$

Thus, we can calculate the density function $g(\varepsilon)$ from the OCV curve using a deconvolution method. In data processing, when $n(\mu)$ and $g(\varepsilon)$ are the datasets consisting of m values, we denote $n(\mu)$ and $g(\varepsilon)$ by $(m \times 1)$ matrices and $f(x)$ by $(m \times m)$ matrix. Because the dataset of $n(\mu)$ is the product of matrices denoting $f(x)$ and $g(\varepsilon)$, we obtain the dataset of $g(\varepsilon)$ by multiplying an inverse matrix of $f(x)$ with the dataset of $n(\mu)$. We calculated the inverse matrix of $f(x)$ by the Gauss–Seidel method so as to yield the dataset of $g(\varepsilon)$.

3.4. Energy distribution of lithium insertion sites

Energy distribution curves of lithium insertion sites were calculated from the discharge curves using Eq. (11), as shown in Fig. 4. Here we assumed that a single phase material was formed by the reaction between Li and TiO_2 and approximately regarded the discharge curves at 0.022 C rate as OCV curves. The abscissa is proportional to the number of insertion sites and the peak area is proportional to the total number of insertion sites. The nanocrystalline anatase TiO_2 showed sharp energy distributions around 2.1 V, indicating that the insertion sites are homogeneous in the host. On the other hand, the amorphous phase had a broad energy distribution from 1.3 V to 3.5 V peaking at about 1.6 V. The site energy $\varepsilon(<0)$ of the amorphous phase was calculated at around −1.6 eV larger than that of the anatase form −2.1 eV. The energy distribution curves as well as the charge/discharge curves indicate that the amorphous phase has a disadvantage in lithium insertion and deinsertion because the insertion sites are energetically and spatially heterogeneous. Here the energy distribution curves were numerically calculated from the discharge curves on the assumption that the repulsive forces among the inserted lithium ions are neglected, and they proved to be very useful to discuss the relationship between crystal structures and discharge properties.

4. Conclusions

Titanium was solubilized into aqueous solution by using a reaction between metallic Ti powder and 30 wt.% aq. H_2O_2 to yield peroxopolytitanic acid (Ti-iPA) solution. Amorphous titanium oxide was obtained as dried residue of Ti-iPA solution at 115 °C, and nanocrystalline anatase titanium oxide was formed by heating the amorphous phase at 300–500 °C. The largest capacity 158 mA h/g as negative electrode for lithium ion batteries was observed for the anatase titanium oxide obtained by heating at 300 °C for 5 h with an average particle size of

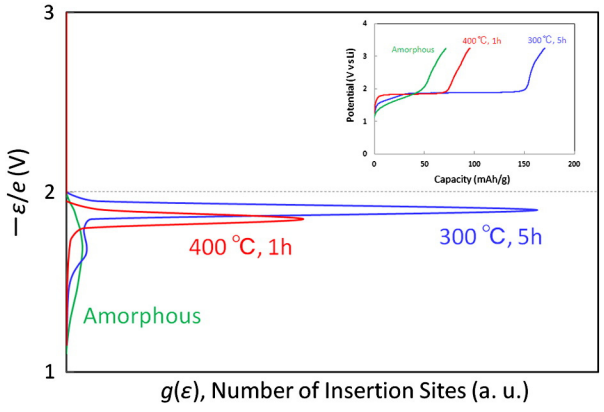

Fig. 4. Energy distribution curves of lithium insertion sites numerically calculated from the discharge curves. The inset shows discharge curves at 0.022 C rate used for theoretical calculations.

25 nm at rather high rate 1.08 C. Any other preparative condition such as shorter heating time at 300 °C and higher temperature 400–500 °C resulted in reduction in capacity, because lattice defects are reduced by heating at 300 °C and crystal growth and aggregation proceed at higher temperature 400–500 °C. In general, nanocrystals with few lattice defects are favorable for lithium insertion and deinsertion, because large surface area and small particle diameter facilitate the lithium diffusion across the electrolyte/electrode interface and inside the particles. Low temperature synthesis is highly desirable for the preparation of electrode materials. We found that heating the amorphous precursor at 300 °C is the most appropriate method for the preparation of anatase titanium oxide for lithium ion batteries. We also presented a theoretical discussion on the relationship between energy distribution of insertion sites and discharge curves, and showed that the energy distribution of insertion sites are numerically calculated from the discharge curves. The nanocrystalline titanium oxide showed uniform site energy distributions reflecting the homogeneous insertion sites, whereas the amorphous phase had a broad energy distribution reflecting the heterogeneous structure. The energy distribution curves calculated from the discharge curves will be very useful to discuss the insertion sites in crystal structures.

Acknowledgments

The authors express their grateful thanks to Dr. Tetsuichi Kudo, Emeritus Professor at the University of Tokyo, for the helpful advice and to Messrs. Kazuki Iwata and Kazuki Sakamoto for their assistance in the experiments in this work.

References

[1] M.P. Cantao, J.I. Cisneros, R.M. Torresi, J. Phys. Chem. 98 (1994) 4865.
[2] W.J. Macklin, R.J. Neat, Solid State Ionics 53–56 (1992) 694.
[3] K. Kanamura, K. Yuasa, Z. Takehara, J. Power Sources 20 (1987) 127.
[4] T. Ohzuku, T. Kodama, T. Hirai, J. Power Sources 14 (1985) 153.
[5] B.A. Morales, O. Novaro, T. Lopez, E. Sanchez, R. Gomez, J. Mater. Res. 10 (1995) 2788.
[6] I. Moriguchi, Y. Shono, H. Yamada, T. Kudo, J. Phys. Chem. B 112 (2008) 14560.
[7] Y. Yagi, M. Hibino, T. Kudo, J. Electrochem. Soc. 144 (1997) 4208.
[8] W. Dong, Y. Sun, C.W. Lee, W. Hua, X. Lu, Y. Shi, S. Zhang, J. Chen, D. Zhao, J. Am. Chem. Soc. 129 (2007) 13894.
[9] L. Kavan, M. Graetzel, J. Rathousky, A. Zukal, J. Electrochem. Soc. 394 (1996) 143.
[10] L. Kavan, K. Kratochvilova, M. Graetzel, J. Electroanal. Chem. 394 (1995) 93.
[11] W. Yue, X. Xu, J.T.S. Irvine, P.S. Attidekou, C. Liu, H. He, D. Zhao, W. Zhou, Chem. Mater. 21 (2009) 2540.
[12] D. Wang, D. Choi, Z. Yang, V.V. Viswanathan, Z. Nie, C. Wang, Y. Song, J.G. Zhang, J. Liu, Chem. Mater. 20 (2008) 3435.
[13] L.D. Noailles, C.S. Johnson, J.T. Vaughey, M.M. Thackeray, J. Power Sources 81–82 (1999) 259.
[14] A. Kuhn, R. Amandi, F. Garcia-Alvarado, J. Power Sources 92 (2001) 221.
[15] M.C. Tsai, J.C. Chang, H.S. Sheu, H.T. Chiu, C.Y. Lee, Chem. Mater. 21 (2009) 499.
[16] M. Zukalova, M. Kalbac, L. Kavan, I. Exnar, M. Graetzel, Chem. Mater. 17 (2005) 1248.
[17] H. Furukawa, M. Hibino, I. Honma, J. Electrochem. Soc. 151 (2004) A257.
[18] M. Wagemaker, W.J.H. Borghois, F.M. Mulder, J. Am. Chem. Soc. 129 (2007) 4323.
[19] M. Hirano, M. Kono, J. Am. Ceram. Soc. 94 (2011) 3319.
[20] M. Gao, Z. Zhang, W. Li, W. Liu, B. Yang, Adv. Mater. Res. 299–300 (2011) 106.
[21] K. Yamamoto, K. Tomita, K. Fujita, M. Kobayashi, V. Petrykin, M. Kakihana, J. Cryst. Growth 311 (2009) 619.
[22] I.J. Clark, T. Takeuchi, N. Ohtori, D.C. Sinclair, J. Mater. Chem. 9 (1999) 83.
[23] A. Verma, A. Basu, A.K. Bakhshi, S.A. Agnihotry, Solid State Ionics 176 (2005) 2285.
[24] T. Yoko, K. Kamiya, A. Yuasa, K. Tanaka, S. Sakka, J. Non-Cryst. Solids 100 (1988) 483.
[25] C. Natarajan, N. Fukunaga, G. Nogami, Thin Solid Films 322 (1998) 6.
[26] A. Aoki, G. Nogami, J. Electrochem. Soc. 143 (1996) L191.
[27] I. Tsuyumoto, K. Kobayashi, ECS Trans. 50 (2013) 17.
[28] I. Tsuyumoto, T. Kato, T. Arai, Mater. Res. Bull. 45 (2010) 1899.
[29] I. Tsuyumoto, M. Kobayashi, T. Are, N. Yamazaki, Chem. Mater. 22 (2010) 3015.
[30] I. Tsuyumoto, K. Nawa, Solid State Ionics 179 (2008) 1227.
[31] I. Tsuyumoto, T. Kudo, Mater. Res. Bull. 31 (1996) 17.
[32] I. Tsuyumoto, T. Kudo, Sensors Actuators B 30 (1996) 95.
[33] I. Tsuyumoto, A. Kishimoto, T. Kudo, Solid State Ionics 59 (1993) 211.
[34] T. Kudo, Y. Sasaki, M. Hashimoto, K. Matsumoto, Inorg. Chim. Acta 145 (1988) 205.
[35] T. Kudo, H. Okamoto, K. Matsumoto, Y. Sasaki, Inorg. Chim. Acta 111 (1986) L27.
[36] T. Kudo, Nature 312 (1984) 537.
[37] F. Izumi, K. Momma, Solid State Phenom. 130 (2007) 15.
[38] C.J. Howard, T.M. Sabine, F. Dickson, Acta Crystallogr. B 47 (1991) 462.
[39] M. Okubo, E. Hosono, J. Kim, M. Enomoto, N. Kojima, T. Kudo, H. Zhou, I. Honma, J. Am. Chem. Soc. 129 (2007) 7444.